NEAR-SURFACE SCATTERING FROM HIGH VELOCITY CARBONATES IN WEST TEXAS

Matthias G. Imhof and M. Nafi Toksöz

Earth Resources Laboratory
Department of Earth, Atmospheric, and Planetary Sciences
Massachusetts Institute of Technology
Cambridge, MA 02139

Charles I. Burch and John H. Queen

Conoco, Inc.
P.O. Box 1267
Ponca City, OK 74602-1267

ABSTRACT

Seismic data acquired directly over near-surface limestone formations are commonly observed to be of inferior quality. A possible cause for this degradation is scattering in the near-subsurface by, e.g., the weathering layer, rough free-surface topography, or heterogeneities such as cavities or clusters of vugs. We applied different numerical scattering schemes to study the effects of each of these three scattering mechanisms. For a particular dataset acquired in West Texas, we find that a weathering layer is the dominant cause of noise on records acquired in valleys. However on mesas, near-subsurface heterogeneity is the primary cause of scattered wave-energy. Topography turned out to be of only secondary importance.

As additional attributes, we use energy-density and energy-flux vectors to study the frequency dependence of the different scattering models. These attributes allow us to study where energy concentrates and in which direction it flows. For example, we observed that near sub-surface heterogeneities build up waveguides which efficiently trap seismic energy near the surface.

INTRODUCTION

In many areas of the world, the nature of the local topography, geomorphology, and geology hinders reflection-seismic exploration. These regions are also called no-record areas. Commonly, it is the presence of high-velocity layers in the near-subsurface which makes it difficult to image deeper structures. Basaltic layers, carbonates outcrops, or permafrost regions are all examples of the problem. Specifically, the problem seems to occur when these high-velocity layers are juxtaposed against much lower velocity

materials. Reflections from depth are almost impossible to interpret on surface seismic data acquired in such regions.

Specialized data acquisition can improve the data quality (Papworth, 1985; Withers *et al.*, 1994; Ryu, 1997). Different processing tools have been applied with varying degrees of success. Pritchett (1990) found that suppressing source-generated noise without also suppressing the desired reflections is rather difficult. On high velocity surfaces, the angle of reflection arrivals at the surface at moderate to long offsets is large, which shortens the apparent horizontal wavelengths of the reflections relative to the wavelengths of some source-generated noise. Papworth (1985) described the application of residual statics using a detailed near-surface velocity model. Purnell (1992) tailored acoustic migration to selected families of converted wave arrivals to image below the high velocity layers. Recently, model-based filters have been developed which remove scattered phases (Blonk and Herman, 1996; Ernst and Herman, 1996).

There are several factors which affect amplitudes and phases. Spatially varying amounts of heterogeneity lead to different static time shifts for each trace (Vandenberghe *et al.*, 1986). Energy trapped in zones of lower velocity causes strong reverberations and yields complex tuning effects (Pujol *et al.*, 1989). Waves are subject to attenuation, absorption, and scattering by the heterogeneities (Wu and Aki, 1985; Gibson and Levander, 1988). Specifically, mode conversions between reflected, transmitted, and surface-waves become very efficient in these situations (Gulati and Stewart, 1997). In the near-subsurface and within waveguides such as low-velocity layers, body waves convert to surface waves and vice versa. Pujol *et al.* (1989) and Papworth (1985) associated strong S-wave arrivals with P-to-S conversion at basalt surfaces. All of these effects affect not only the original P-wave, but also source-generated noise and reflections from deeper layers.

We acquired a dataset in West Texas over high-velocity carbonate formations. As examples, two shot gathers are shown in Figures 1 and 2. The first record (Figure 1) was acquired in a topographic depression. The second record (Figure 2) is recorded on top of a mesa. Both records are badly contaminated by 'noise'. Our data-processors reported a number of problems, including statics, the weathering layer, and topographic effects. Interestingly, they considered their main problem to be backscattered wave-energy over the mesas. The backscattered energy could not be removed by conventional processing. The amount of scattered energy was simply too large and incoherent.

In this paper, we do not attempt to derive alternative acquisition or processing schemes. We believe that the first step in understanding the problem is to identify its cause and to study what exactly happens when seismic waves pass through such regions. Hence, we develop different geological models for the near-subsurface. Specifically, we consider three different scattering mechanisms: (1) strongly heterogeneous debris or weathering layers; (2) irregular topography; and (3) heterogeneities such as large vugular cavities. Because we are mainly interested in the qualitative behavior of the different mechanisms, we limit ourselves to 2-D models and 2-D propagation. For each model, we calculate synthetic seismograms and compare its results to our field records. We find

that the weathering layer (1) is the dominant cause of degradation for data acquired over topographical depressions. Contrarily, we find near-subsurface heterogeneities (3), such as cavities and other regions of enhanced porosity, to be the primary cause of scattering for data acquired over elevated areas.

This paper is structered as follows: First, we look at the field data, study how data quality and topography correlate, and present the three mechanisms. We calculate the synthetic seismogram for an equivalent flat free-surface model which serves as reference data for comparisons. Second, we use a boundary element method, described in Appendix A, to calculate the seismogram for rough free-surface topography. Then, we simulate the effects of heterogeneities at various levels of depth using the Multiple Multipole Method, described in Appendices B and C. As additional attributes, we will use frequency dependent energy-density and energy-flux to study where energy concentrates and where it propagates. Finally, we will discuss and summarize our findings.

WEST TEXAS DATASET

Conoco acquired the dataset in West Texas over Cretaceous formations. Unfortunately, they did not release complete or detailed information. For example, neither the exact location nor the applied source- and receiver-patterns have been disclosed. Figure 3 presents the elevation of source- and receiver-stations relative to an unknown datum. Two distinct levels can be seen: Elevations over 1750 ft are on mesas. Experience suggests that mesas are hard formations. Contrarily, elevations below 1750 ft constitute valleys. It is likely that they are covered with debris comprising a very heterogeneous near-surface layer.

Not surprisingly, seismic records acquired over the valley region differ drastically from records acquired on a mesa. For example, the seismogram shown in Figure 1 was shot across the valley with the source located at station 1045. The other seismogram (Figure 2) was recorded on top of the mesa with the source located at station 1153. The two regions differ most significantly in the appearance of the Rayleigh waves. The valley record 1045 contains some Rayleigh waves, especially for later arrival times and larger offsets, but it is an incoherent event with nonlinear traveltimes. However, the Rayleigh waves dominate on mesa record 1153, with linear traveltime and consistent amplitudes. A similar difference is observed for the first breaks. In the valley record 1045, the first break is a fading event strongly affected by static shifts. In the mesa record 1153, it is a rather strong and very linear feature.

From records acquired on top of the mesa, we estimated average seismic velocities of the surface layer: P-wave velocity $\alpha = 4630\,\mathrm{m/s}$, S-wave velocity $\beta = 2122\,\mathrm{m/s}$, and Rayleigh wave velocity $\gamma = 1990\,\mathrm{m/s}$. The velocities of P- and Rayleigh waves are directly measured from the records, while the S-wave velocity is inferred from the

Rayleigh function for a uniform, elastic halfspace (Aki and Richards, 1980).

$$\frac{\gamma^2}{\beta^2}\left[\frac{\gamma^6}{\beta^6} - 8\frac{\gamma^4}{\beta^4} + \left(24 - 16\frac{\beta^2}{\alpha^2}\right)\frac{\gamma^2}{\beta^2} - 16\left(1 - \frac{\beta^2}{\alpha^2}\right)\right] = 0. \tag{1}$$

From the data, we also obtain the dominant frequency of 30 Hz. For the density ρ, we will use an average limestone density of 2600 kg/m^3 (Clark, 1966).

The data-processors reported a number of problems, including statics, the weathering layer, and topographic effects. For data acquired over the valley fill, standard processing sequences were found to be marginally successful in imaging deeper reflections. They considered their main problem to be backscattered P- and Rayleigh waves on records acquired over the mesas. These events could not be removed by conventional processing. The amount of incoherent energy was simply too large. To examine this further, we used a slant stack to separate forward and backward propagating wave-energy (Durrani and Bisset, 1984). Figure 4 shows the top portion of the first 56 traces from the record shot over the mesa. Also shown are the forward/backward separated records. All three seismograms are scaled equally. Interestingly, hardly any backscattered Rayleigh waves can be detected in Figure 4(c). Nearly all backscattered events propagate with the P-wave velocity. They mostly radiate from the direct and near-surface guided P-wave.

To understand these effects, we need to consider the morphology and geology of the outcropping carbonates. We devised three different models which could explain the observed degradation of the seismic signal: (1) strongly heterogeneous debris or weathering layers; (2) rough surface topography; and (3) near-surface heterogeneities such as large vugular cavities and regions of enhanced porosity. Weathering layers are conceptionally very similar to the third mechanism. One expects variable amounts of static delays and conversion of different wavemodes. However, the effect of the two models is quite different. Robertsson *et al.* (1996) examined the effect of strongly heterogeneous weathering layers. Using a finite difference model, they observed the formation of waveguides. While their results do not resemble our mesa record 1153, their seismograms look very much like our valley record 1045! This observation appears reasonable. The formation of a thick weathering layer is much more likely in a topographical depression (valley) than on an elevation (mesa).

Rough topography is known to cause significant effects of amplification and deamplification of propagating waves both at the irregularity itself and in a substantial neighborhood around it. Rough surface topography also converts wavemodes very efficiently, generating strong backscattered waves (Sanchez-Sesma and Campillo, 1991).

Commonly, near-surface limestone layers are highly heterogeneous, despite their massive appearance. Although the matrix velocity is rather high, these layers often contain a substantial amount of pore space which may contain low-velocity materials such as gases, liquids, or soil. A wave propagating through such a layer is delayed by variable amounts, yielding problems with statics (Vandenberghe *et al.*, 1986; Mukerji *et al.*, 1995). Furthermore, mode conversions of reflected, transmitted, and surface waves become very efficient in these situations.

Since the processing of data acquired over valleys was marginally successful, we will focus our study on the mesas concentrating on mechanisms (2), rough surface topography, and (3), near-surface heterogeneities such as large vugular cavities and regions of enhanced porosity. Using the method of discrete wavenumber integration (Bouchon and Aki, 1977), we calculate the response of a homogeneous limestone halfspace. Not knowing the exact acquisition geometry, we assume an explosive point-source at a depth of 10 m and point-receivers 1 m below the surface. We use a Ricker wavelet (Hosken, 1988) with a center-frequency of 30 Hz as source-time function. Figure 5 presents the z-component of the synthetic seismogram which should be compared to the enlarged mesa record 1153 shown in Figure 4(a). Clearly, the timings of the first break and the Rayleigh wave are correct. Not surprisingly, the synthetic record misses all other arrivals visible on the field record.

As additional quantities, we also define the time averaged energy-flux vector and the energy-density of the wavefields (Ben-Menahem and Singh, 1981). The instantaneous energy-flux vector $\mathbf{S}(\mathbf{x},t)$, also known as Poynting power, is defined by

$$\mathbf{S}(\mathbf{x},t) = \Re e\, \boldsymbol{\sigma}(\mathbf{x},t) \cdot \Re e\, \dot{\mathbf{u}}(\mathbf{x},t) \tag{2}$$

where the dot denotes the derivative with respect to time. For a harmonic wave of angular frequency ω, we easily obtain the time averaged energy-flux vector $\mathbf{S}(\mathbf{x},\omega)$:

$$\begin{aligned} \mathbf{S}(\mathbf{x},\omega) &= \big\langle \mathbf{S}(\mathbf{x},t) \big\rangle \\ &= \frac{1}{T} \int_0^T \mathbf{S}(\mathbf{x},t)\, dt \\ &= \frac{i\omega}{4} \big(\boldsymbol{\sigma}^*(\mathbf{x},\omega) \cdot \mathbf{u}(\mathbf{x},\omega) - \boldsymbol{\sigma}(\mathbf{x},\omega) \cdot \mathbf{u}^*(\mathbf{x},\omega) \big) \,. \end{aligned} \tag{3}$$

The superscript * denotes the complex conjugate. $\boldsymbol{\sigma}(\mathbf{x})$ is the stress tensor associated with the displacement field $\mathbf{u}(\mathbf{x},\omega)$. The energy-flux provides a measure of how much energy flows in a given direction. Plotted as a vector field, it also shows the coherency of the wavefield. We also define another quantity, the energy-density $E(\mathbf{x},\omega)$:

$$\begin{aligned} E(\mathbf{x},\omega) &= \frac{\rho(\mathbf{x})}{2}\, \dot{\mathbf{u}}(\mathbf{x},\omega) \cdot \dot{\mathbf{u}}^*(\mathbf{x},\omega) + \frac{1}{2}\, \boldsymbol{\sigma}(\mathbf{x},\omega) : \boldsymbol{\varepsilon}^*(\mathbf{x},\omega) \\ &= \rho(\mathbf{x})\, \dot{\mathbf{u}}(\mathbf{x},\omega) \cdot \dot{\mathbf{u}}^*(\mathbf{x},\omega) \\ &= \omega^2 \rho(\mathbf{x})\, \mathbf{u}(\mathbf{x},\omega) \cdot \mathbf{u}^*(\mathbf{x},\omega) \end{aligned} \tag{4}$$

$\boldsymbol{\varepsilon}(\mathbf{x})$ is the strain tensor associated with the displacement field $\mathbf{u}(\mathbf{x},\omega)$. We simplified the expression using the equipartition theorem between kinetic- and strain-energy-density (Aki and Richards, 1980) which allows us to use only one term, the kinetic, which is easier to evaluate. The energy-density $E(\mathbf{x},\omega)$ reveals where energy is concentrated. Both energy-flux and energy-density are frequency dependent. For the flat free-surface, we calculate the two measures at two different frequencies, 20 Hz and 45 Hz. The results are shown in Figure 6. The arrows show magnitude and direction of the energy-flux. At

both frequencies, energy is predominantly flowing downward and along the free surface. The color-shading shows the energy-density. Bright colors denote higher energies, while dim colors denote lower ones. We observe that energy is highly concentrated along two lobes, similar to a vertical point-force, and along the free surface. The wiggling of the energy-flux vectors and the checkerboard pattern of the energy-density are not numerical artifacts but interference effects between direct P-, reflected P-, converted S-, and the Rayleigh-wave which have different spatial wavelengths. It is well-known that linear superposition of different wavelengths yields spatial beating patterns. Note that the wavelength of the beat at 20 Hz is nearly twice the beating wavelength at 45 Hz.

IRREGULAR TOPOGRAPHY

Irregular topography is known to cause amplification and deamplification of propagating waves both at the irregularity itself and in a substantial neighborhood around it. Rough surface topography also converts wavemodes very efficiently, generating strong backscattered waves (Sanchez-Sesma and Campillo, 1991). To study the effect of the topography depicted in Figure 3, we apply a boundary element technique similar to the one developed by Sanchez-Sesma and Campillo. We assume that the total wavefield $\mathbf{u}^{tot}(\mathbf{x},\omega)$ can be separated into an incident field $\mathbf{u}^{inc}(\mathbf{x},\omega)$ and a diffracted field $\mathbf{u}^{diff}(\mathbf{x},\omega)$ induced by the rough topography. Applying Huygen's principle, we postulate a set of forces $\eta(\mathbf{x}',\omega)$, acting as secondary sources, at every point $\mathbf{x}'$ along the interface. We write the total wavefield as

$$\mathbf{u}^{tot}(\mathbf{x},\omega) = \mathbf{u}^{inc}(\mathbf{x},\omega) + \int \mathbf{G}(\mathbf{x},\mathbf{x}',\omega)\cdot\eta(\mathbf{x}',\omega)\,d\mathbf{x}' \qquad (5)$$

where $\mathbf{G}(\mathbf{x},\mathbf{x}',\omega)$ is the displacement Green's tensor for a force system at location $\mathbf{x}'$ evaluated at $\mathbf{x}$. Discretizing the force system $\eta(\mathbf{x},\omega)$ and the free-surface boundary condition allows us to solve the integral equation (5) for each frequency ω. Once $\eta(\mathbf{x},\omega)$ is determined, we calculate energy-density $E(\mathbf{x},\omega)$, energy-flux $\mathbf{S}(\mathbf{x},\omega)$, and by Fourier synthesis seismograms $\mathbf{u}(\mathbf{x},t)$. The method is outlined in greater detail in Appendix A.

Figure 7 shows the vertical displacement calculated for the topography of the mesa record 1153. While the flat free-surface yielded only the 'direct' P arrival and a strong Rayleigh wave (Figure 5), we now obtain multiple P-wave arrivals in the forward direction and various Rayleigh arrivals propagating both forwards and backwards. Figure 8 shows the energy-density $E(\mathbf{x},\omega)$ and energy-flux vectors $\mathbf{S}(\mathbf{x},\omega)$ for 20 Hz and 45 Hz. The same scaling was applied as for the flat free-surface case shown in Figure 6—the bright yellow color indicates pixels laying above the rough topography. At 20 Hz, energy-density and energy-flux are similar to the flat free-surface case. One would expect this result. In terms of the dominant spatial wavelengths, the rough topography is merely a small perturbation of the flat free-surface. At 45 Hz, the differences between the flat and the rough surface are more distinct. In general, the energy-densities are smaller for the case of the rough surface. For larger offsets, the energy-distribution patterns shift downwards by the average amount of topography above.

Compared with the field record 1153 shown in Figure 4(a), the rough topography generates too many scattered Rayleigh waves while hardly producing any scattered P-waves, which dominate the field record. Based on this observation, we exclude rough surface topography as the major mechanism for generating scattered energy contaminating the records acquired over West Texas mesas.

NEAR-SUBSURFACE HETEROGENEITIES

The third and final mechanism to be considered is strong heterogeneities in the near-subsurface, e.g. vugs, joints, cavities, or other regions of enhanced porosity. Commonly, these features cluster and align along fault-planes or structural boundaries. To model waves propagating in such environments, we adapt the Multiple MultiPoles method (MMP) which is particularly well suited for elastic scattering from individual heterogeneities or clusters thereof approaching a sizable portion of the dominant seismic wavelength. The method has been described in detail in a previous publication (Imhof, 1996). In Appendix B, we outline the method only as necessary for the present work. We separate the total wavefield $\mathbf{u}^{tot}(\mathbf{x},\omega)$ into the incident field $\mathbf{u}^{inc}(\mathbf{x},\omega)$ and a field $\mathbf{u}^{diff}(\mathbf{x},\omega)$ scattered by the heterogeneities. The scattered wavefield is expanded into a set of basis functions which are solutions to the wave equation in a homogeneous reference medium. Assuming we have D heterogeneities, the displacement $\mathbf{u}^{diff}(\mathbf{x},\omega)$ of the scatterered wavefield can be expressed as

$$\mathbf{u}^{diff}(\mathbf{x},\omega) = \sum_{d=1}^{D} \sum_{p=1}^{P_d} \sum_{n=-N}^{+N} a_{pnd}\, \mathbf{u}^{\Phi}_{pnd}(\mathbf{x},\mathbf{x}_{pd},k,\omega) + b_{pnd}\, \mathbf{u}^{\Psi}_{pnd}(\mathbf{x},\mathbf{x}_{pd},l,\omega)\,. \qquad (6)$$

For a fullspace, the expansion functions $\mathbf{u}^{\Phi}_{pnd}$ and $\mathbf{u}^{\Psi}_{pnd}$ are given in terms of scalar multipole potentials (B-4). For the present problem, we need expansions which also contain the effect of the free surface. We will use asymptotic expansions (C-23) and (C-24) which are derived in Appendix C. Equations for the weighting coefficients a_{pnd} and b_{pnd} are found by enforcing the boundary condition at discrete points along the interfaces between elastic halfspace and void inclusions. These equations form a system of linear equations, which determine the self-consistent solution to the posed scattering problem.

The models consist of elliptical heterogeneities (4 m × 2 m) embedded in a homogeneous halfspace. For simplicity, we define the heterogeneities to be voids. Each heterogeneity represents a cluster of vugs, joints and cavities, or any other region of enhanced porosity. They are aligned around a common depth. We will calculate two different models with average depths of 25 m and 80 m, respectively. The depth variance is 3 m, the average horizontal separation is 15 m, and the horizontal variance is 5 m. Special care has been taken to avoid overlap between different heterogeneities as overlap would break our numerical scheme. For both models, we calculate the vertical displacement. The seismograms are presented in Figure 9. Both cases have the

direct P-wave and the dominant Rayleigh wave in common. However, the scattered fields are very different. Shallow heterogeneities generate predominantly backscattered Rayleigh waves emanating from the original Rayleigh wave. To a lesser degree, they also radiate forward scattered Rayleigh waves originating from the direct P-wave. Deep heterogeneities primarily generate P-waves that propagate in the backward direction. The scattered waves originate from the body-waves. These effects are to be expected because the Rayleigh waves do not go deep enough to be scattered by heterogeneities. Likewise, the scatterers are too deep to generate large amounts of Rayleigh waves.

We obtain further insight from energy-density $E(\mathbf{x}, \omega)$ and energy-flux $\mathbf{S}(\mathbf{x}, \omega)$. Figure 10 shows these quantities for shallow heterogeneities at 20 Hz and 45 Hz. Again, the scales equal the ones applied in the previous figures. Wave-energy is effectively trapped between the free-surface and the heterogeneities. The heterogeneities act like a waveguide, enhancing propagation along the surface. However, this effect is not uniform—at some locations energy-density increases, while at others it decreases. Downwards, energy is being passed in only a few directions. Altogether, the heterogeneities form a screen and reduce the coherence of the wavefields. For deep heterogeneities the results are slightly different (Figure 11). At 20 Hz, the energy-density is hardly affected by the presence of the scatterers. Their distance from the seismic source is large enough that wave propagation is barely disturbed. At 45 Hz, the situation is different. The seismic wavelengths are closer to dimension and separation of the heterogeneities. As for shallow heterogeneities, energy is being trapped between the free-surface and the scatterers, and coherence of the energy-flux is reduced. Again, the heterogeneities are building up a waveguide.

The synthetic seismogram calculated for the model with the deep heterogeneities, shown in Figure 9(b), exhibits features very similar to the ones observed over the mesa record 1153 shown (Figure 4). We believe that heterogeneity at some depth below the surface causes the degradations observed on the records acquired over the mesas.

DISCUSSION AND CONCLUSIONS

All numerical simulations were done in 2-D. In order to apply these simulations to 3-D, the properties of wave propagation and scattering need to be compared for 2-D and 3-D waves. As 2-D waves propagate, their amplitude varies and the wavelet changes its shape. Because we never used amplitude in this study, and we are concerned only with qualitative behavior of near sub-surface heterogeneity models, these differences are insignificant.

All three models of heterogeneity vary in 3-D with each model generating more, and possibly stronger, events for 3-D propagation and 3-D models. Although results will be contaminated by scattered energy, the general, qualitative findings will remain the same. Therefore, despite variation both in wave propagation and in scattering, the numerical simulations of this study can be applied to 3-D wave propagation.

We found that the effects of rough surface topography and near-subsurface hetero-

geneities are frequency dependent. Higher frequencies (45 Hz) are much more affected than lower ones (20 Hz). For example, the scattering strength strongly depends on the ratio between characteristic size of the heterogeneities and the dominant wavelength (Aki and Richards, 1980). This dependence implies that different frequency components of the wavefield scatter differently thus both reducing the coherence of the different phases and reflections and contributing to source generated background noise. The frequency dependence also results in dispersion and apparent attenuation.

For aligned heterogeneity in the near-subsurface, we found that wave-energy is efficiently being trapped between heterogeneities and the free-surface. We observed that aligned heterogeneities forms waveguides. Further from the surface, the wavefield propagating downwards is noisy and incoherent. Moreover, reflections from deeper targets propagate back through this layer, degrading the sought reflections once more.

In the example seismic dataset, we find that the quality of the data depends strongly on the location of source and receivers with respect to valleys and mesas. We began with the assumption that scattering was responsible for these differences. We proposed three different scattering mechanisms: (1) strongly heterogeneous debris or weathering layers; (2) irregular topography; and (3) near-surface heterogeneities such as cavities or regions of enhanced porosity. A comparison of Figure 1 against results obtained by Robertsson *et al.* (1996) made us believe that mechanism (1) is dominant for data acquired in the valleys. However, data acquired on top of seismically-fast limestone mesas proved to be of even lower quality, e.g., Figure 2. A very strong Rayleigh wave and large amounts of scattered wave-energy dominate the records, overwhelming reflections from deeper targets. By comparing synthetic seismograms with field data, we ranked mechanism (1) to be the least important and (3) to be the most important. We found scattered wave-energy to be predominantly in the form of P-waves which suggests that the heterogeneities are located not directly at the surface but at some depth, e.g., 80 m. Due to their common presence in outcropping limestone, we believe that small cavities, vugs, or other regions of enhanced porosity are the cause of the observed degradation of seismic signals recorded in West Texas.

ACKNOWLEDGMENTS

This work was supported by the Borehole Acoustics and Logging/Reservoir Delineation Consortia at the Massachusetts Institute of Technology.

References

Abramowitz, M. and Stegun, I.A. (editors), 1964, *Handbook of Mathematical Functions*, Dover, New York.

Aki, K. and Richards, P.G, 1980, *Quantitative Seismology: Theory and Methods*, Freeman, San Francisco, CA.

Ben-Menahem, A. and Singh, S.J., 1981, *Seismic Waves and Sources*, Springer, New York.

Blonk, B. and Herman, G, 1996, Removal of scattered surface waves using multicomponent seismic data, *Geophysics, 61*, 1483–1488.

Bouchon, M. and Aki, K., 1977, Discrete wavenumber representation of seismic-source wave fields, *Bull. Seismol. Soc. Am., 67*, 259–277.

Chew, W.C., 1990, *Waves and Fields in Inhomogeneous Media*, Van Nostrand Reinhold, New York.

Clark, S.P. (editor), 1966, *Handbook of Physical Constants*, Geological Society of America, New York.

DeSanto, J.A., 1992, *Scalar Wave Theory*, Springer, New York.

Durrani, T.S. and Bisset, D., 1984, The radon transform and its properties, *Geophysics, 49*, 1180–1187.

Ernst, F.E. and Herman, G.C., 1996, Imaging of scattered guided waves in heterogeneous media, In *66th SEG Annual Meeting Expanded Technical Program Abstracts, 96*, 1955–1958.

Gibson, B.S. and Levander, A.R., 1988, Modeling and processing of scattered waves in seismic reflection surveys, *Geophysics, 53*, 466–478.

Gulati, J.G. and Stewart, R.R., 1997, Seismic exploration through high-velocity layers, In *67th SEG Annual Meeting Expanded Technical Program Abstracts, 67*, 1297–1300.

Hosken, J.W., 1988, Ricker wavelets in their various guises, *First Break, 6*, 24–33.

Imhof, M.G., 1996, Multiple multipole expansions for elastic scattering, *J. Acoust. Soc. Am., 100*, 2969–2979.

Lapwood, E.R., 1949, The disturbance due to a line source in a semi-infinite elastic medium, *Philosophical Transactions of the Royal Society of London, A242*, 63–100.

Mukerji, T., Mavko, G., Mujica, D., and Lucet, N., 1995, Scale-dependent seismic velocity in heterogeneous media, *Geophysics, 60*, 1222–1233.

Papworth, T.J., 1985, Seismic exploration over basalt covered areas in the U.K., *First Break, 3*, 20–32.

Press, W.H., Flannery, B.P., Teukolsky, S.A., and Vetterling, W.T., 1988, *Numerical Recipes*, Cambridge Press, Cambridge, U.K.

Pritchett, W.C., 1990, Problems and answers in recording reflections from beneath karst or volcanic surfaces, In *60th SEG Annual Meeting Expanded Technical Program Abstracts, 90*, 922–925.

Pujol, J., Fuller, B.N., and Smithson, S.B., 1989, Interpretation of a vertical seismic profile conducted in the Columbia Plateau basalts, *Geophysics, 54*, 1258–1266.

Purnell, G.W., 1992, Imaging beneath a high-velocity layer using converted waves, *Geophysics, 57*, 1444–1452.

Robertsson, J.O.A., Holliger, K., Green, A.G., Pugin, A., and Iaco, R.D., 1996, Effects of near-surface waveguides on shallow high-resolution seismic refraction and reflection data, *Geophysical Research Letters, 23*, 495–498.

Ryu, J.V., 1997, Seeing through seismically difficult rock unconventionally, *Geophysics, 62*, 1177–1182.

Sanchez-Sesma, F.J. and Campillo, M., 1991, Diffraction of P, SV, and Rayleigh waves by topographic features: a boundary integral formulation, *Bull. Seismol. Soc. Am., 81*, 2234–2253.

Vandenberghe, N., Poggiagliolmi, E., and Watts, G., 1986, Offset-dependent seismic amplitudes from karst limestone in northern Belgium, *First Break, 4*, 9–27.

Withers, R., Eggers, D., Fox, T., and Crebs, T, 1994, A case study of integrated hydrocarbon exploration through basalt, *Geophysics, 59*, 1666–1679.

Wu, R.S. and Aki, K., 1985, Elastic wave scattering by a random medium and small-scale inhomogeneities in the lithosphere, *J. Geophys. Res., 90*, 10261–10273.

Appendix A Boundary Element Method

Following the derivation by Sanchez-Sesma and Campillo (1991), we assume that the total wavefield $\mathbf{u}^{tot}(\mathbf{x},\omega)$ can be separated into an incident field $\mathbf{u}^{inc}(\mathbf{x},\omega)$ and a diffracted field $\mathbf{u}^{diff}(\mathbf{x},\omega)$ induced by the rough topography.

$$\mathbf{u}^{tot}(\mathbf{x},\omega) = \mathbf{u}^{inc}(\mathbf{x},\omega) + \mathbf{u}^{diff}(\mathbf{x},\omega) \tag{A-1}$$

Applying Huygen's principle, we define the diffracted field by a set of forces $\boldsymbol{\eta}(\mathbf{x}',\omega)$ acting as secondary sources at every point $\mathbf{x}'$ along the interface. As a notational detail, we assume primed coordinates to be on the free surface. Unprimed coordinates are anywhere in the elastic halfspace.

$$\mathbf{u}^{tot}(\mathbf{x},\omega) = \mathbf{u}^{inc}(\mathbf{x},\omega) + \int \mathbf{G}(\mathbf{x},\mathbf{x}',\omega)\cdot\boldsymbol{\eta}(\mathbf{x}',\omega)\,d\mathbf{x}' \tag{A-2}$$

where $\mathbf{G}(\mathbf{x},\mathbf{x}',\omega)$ is the displacement Green's tensor for a force system located at $\mathbf{x}'$ evaluated at $\mathbf{x}$. The displacement Green's tensor is given by (Ben-Menahem and Singh, 1981)

$$\mathbf{G}(\mathbf{x},\mathbf{x}',\omega) = \frac{1}{\rho\omega^2}\Big[l^2\mathbf{I}\psi(lr) + \nabla\nabla\big(\psi(lr)-\phi(kr)\big)\Big] \tag{A-3}$$

where ρ is the density, ω defines the angular frequency, $k=\omega/\alpha$ and $l=\omega/\beta$ denote wavenumbers for the P- and S-waves, $r=|\mathbf{x}-\mathbf{x}'|$, and finally the scalar Green's functions $\phi(kr) = iH_0^{(1)}(kr)/4$ and $\psi(lr) = iH_0^{(1)}(lr)/4$ with $H_0^{(1)}(\cdot)$ the Hankel functions of the first kind and zeroth order. The traction-free boundary condition at the free surface $\mathbf{x}''$ implies that

$$\mathbf{t}^{inc}(\mathbf{x}'',\omega) + \frac{1}{2}\boldsymbol{\eta}(\mathbf{x}'',\omega) + \int \mathbf{T}(\mathbf{x}'',\mathbf{x}',\omega)\cdot\boldsymbol{\eta}(\mathbf{x}',\omega)\,d\mathbf{x}' = \mathbf{0} \tag{A-4}$$

where $\mathbf{t}^{inc}(\mathbf{x}'',\omega)$ is the traction of the incident wave. The term $1/2\boldsymbol{\eta}(\mathbf{x}'',\omega)$ accounts for the singularity of the traction at $\mathbf{x}'=\mathbf{x}''$. The tensor $\mathbf{T}(\mathbf{x}'',\mathbf{x}',\omega)$ yields the traction at $\mathbf{x}''$ in the direction $\hat{\mathbf{n}}(\mathbf{x}'')$ for a force system located at $\mathbf{x}'$. $\mathbf{T}$ can be obtained from the displacement Green's tensor $\mathbf{G}$ by the relations between displacement, strain, and stress

$$\mathbf{T}(\mathbf{x}'',\mathbf{x}',\omega) = \frac{1}{2}\mathbf{C} : \big(\nabla\mathbf{G}(\mathbf{x}'',\mathbf{x}',\omega) + \mathbf{G}(\mathbf{x}'',\mathbf{x}',\omega)\nabla\big)\cdot\hat{\mathbf{n}}(\mathbf{x}'') \tag{A-5}$$

where $\mathbf{C}$ is the fourth-order compliance tensor containing the elastic material parameters. Discretizing the integral equation (A-4) yields a matrix equation for the yet unknown forces $\boldsymbol{\eta}(\mathbf{x}',\omega)$. First, we limit the integration boundaries to $\pm L/2$ where the distance L is large enough that truncation effects do not reach the receivers within the time window of interest. Second, we split the range between $\pm L/2$ into N elements of

length $\Delta s = L/N = \mathbf{x}'_n - \mathbf{x}'_{n-1}$ where the coordinates $\mathbf{x}'_n$ are the midpoints of the little elements. Finally, we assume the force $\eta(\mathbf{x}', \omega)$ to be of the form

$$\eta(\mathbf{x}', \omega) = \sum_{n=1}^{N} W(\mathbf{x}'_n - \mathbf{x}')\eta_n(\omega) \tag{A-6}$$

where $W(\mathbf{x})$ are triangular shape functions which yield a piecewise-linear approximation of the forces $\eta(\mathbf{x}', \omega)$:

$$W(\mathbf{x}) = \begin{cases} 1 - |\mathbf{x}|/\Delta s & \text{for} |\mathbf{x}| < \Delta s \\ 0 & \text{for} |\mathbf{x}| > \Delta s \end{cases} . \tag{A-7}$$

The grand integral (A-4) is converted into a summation of integrals over the shape functions which can be evaluated by Gaussian integration of order J with weighting coefficients w_j and nodal points ξ_j.

$$\begin{aligned} -\mathbf{t}^{inc}(\mathbf{x}''_m, \omega) &= \frac{1}{2}\eta(\mathbf{x}''_m, \omega) + \int \mathbf{T}(\mathbf{x}''_m, \mathbf{x}', \omega) \cdot \eta(\mathbf{x}', \omega)\, d\mathbf{x}' \\ &= \frac{1}{2}\eta_m(\omega)\delta_{mn} + \sum_{n=1}^{N} \int \mathbf{T}(\mathbf{x}''_m, \mathbf{x}', \omega) \cdot W(\mathbf{x}''_n - \mathbf{x}')\eta_n(\omega)\, d\mathbf{x}' \\ &= \frac{1}{2}\eta_m(\omega)\delta_{mn} + \Delta s \sum_{n=1}^{N} \Big\{ \sum_{j=1}^{J} w_j\, \mathbf{T}(\mathbf{x}''_m, \mathbf{x}'_n + \xi_j, \omega) \Big\} \cdot \eta_n(\omega) \end{aligned} \tag{A-8}$$

Every midpoint $\mathbf{x}'_n$ is used once as $\mathbf{x}''_m$ which yields a set of matrix equations for the discrete forces $\eta_n(\omega)$.

Appendix B Elastic Multiple Multipole Expansions

In this appendix, we want to state some of the main features of the Multiple MultiPole (MMP) method which was presented in another publication (Imhof, 1996) and how we applied those features. The medium is assumed to be a homogeneous fullspace with D embedded cavities. In the frequency domain, the displacement $\mathbf{u}(\mathbf{x}, \omega)e^{i\omega t}$ of an elastic P-SV wave travelling in the two dimensional, homogeneous region is described by

$$\frac{1}{k^2}\nabla\nabla \cdot \mathbf{u} - \frac{1}{l^2}\nabla \times \nabla \times \mathbf{u} + \mathbf{u} = 0 \tag{B-1}$$

where we suppressed the harmonic time factor $e^{i\omega t}$. We also introduced the wave vectors $k = \omega/\alpha$ and $l = \omega/\beta$ for a particular frequency ω, P-wave velocity α, and S-wave velocity β.

Instead of directly using the displacement $\mathbf{u}^{tot}(\mathbf{x}, \omega)$, we separate it into parts.

$$\mathbf{u}^{tot}(\mathbf{x}, \omega) = \mathbf{u}^{inc}(\mathbf{x}, \omega) + \mathbf{u}^{diff}(\mathbf{x}, \omega) = \mathbf{u}^{inc}(\mathbf{x}, \omega) + \mathbf{u}^{\Phi}(\mathbf{x}, \omega) + \mathbf{u}^{\Psi}(\mathbf{x}, \omega) + \mathbf{u}^{\epsilon}(\mathbf{x}, \omega) \tag{B-2}$$

The first term $\mathbf{u}^{inc}(\mathbf{x},\omega)$ is the incident wavefield. The terms $\mathbf{u}^{\Phi}$ and $\mathbf{u}^{\Psi}$ denote the P- and S-waves generated by the cavities. Because they depend on the geometry of the cavities and the source mechanism, we will expand them into multiple multipole series. We will need to truncate the expansions after a finite number of terms. Therefore, we also add an error term $\mathbf{u}^{\varepsilon}(\mathbf{x},\omega)$ to (B-2).

The displacement fields $\mathbf{u}^{\Phi}$ and $\mathbf{u}^{\Psi}$ are expanded as follows:

$$\mathbf{u}^{\Phi}(\mathbf{x},\omega) = \sum_{d=1}^{D}\sum_{p=1}^{P_d}\sum_{n=-N}^{+N} a_{pnd}\,\mathbf{u}^{\Phi}_{pnd}(\mathbf{x},\mathbf{x}_{pd},k,\omega)\,, \tag{B-3a}$$

$$\mathbf{u}^{\Psi}(\mathbf{x},\omega) = \sum_{d=1}^{D}\sum_{p=1}^{P_d}\sum_{n=-N}^{+N} b_{pnd}\,\mathbf{u}^{\Psi}_{pnd}(\mathbf{x},\mathbf{x}_{pd},l,\omega)\,, \tag{B-3b}$$

where a_{pnd} and b_{pnd} are yet unknown weighting coefficients. The expansion functions $\mathbf{u}^{\Phi}_{pnd}$ and $\mathbf{u}^{\Psi}_{pnd}$ are solutions to (B-1). We have an expansion for each cavity $1 \le d \le D$. In each cavity d, we place P_d different multipoles of orders $-N$ to $+N$ centered at $\mathbf{x}_{pd}$. Each summation over n corresponds to a multipole. Because we have more than one multipole per cavity, the scheme is named multiple multipoles expansion. For a homogeneous fullspace, the expansion functions are defined as:

$$\mathbf{u}^{\Phi}_{pnd}(\mathbf{x},\mathbf{x}_{pd},k,\omega) = \nabla H^{(1)}_{|n|}\left(k\,|\mathbf{x}-\mathbf{x}_{pd}|\right) e^{in\vartheta_{pd}} \tag{B-4a}$$

$$\mathbf{u}^{\Phi}_{pnd}(\mathbf{x},\mathbf{x}_{pd},l,\omega) = \nabla \times \hat{\mathbf{y}} H^{(1)}_{|n|}\left(l\,|\mathbf{x}-\mathbf{x}_{pd}|\right) e^{in\vartheta_{pd}} \tag{B-4b}$$

For a halfspace, we add the steepest-descend contributions of the free surface to the expansions. The resulting expansions (C-23) and (C-24) are derived in Appendix C. Each expansion function satisfies the wave equation (B-1). For each function, e.g. $\mathbf{u}^{\Phi}_{pnd}$, we obtain the corresponding stress tensor $\boldsymbol{\sigma}^{\Phi}_{pnd}$:

$$\boldsymbol{\sigma}^{\Phi}_{pnd} = \frac{1}{2}\mathbf{C} : \left(\nabla \mathbf{u}^{\Phi}_{pnd} + \mathbf{u}^{\Phi}_{pnd}\nabla\right), \tag{B-5}$$

where $\mathbf{C}$ is a fourth-order tensor containing the elastic parameters (Ben-Menahem and Singh, 1981). On the boundary of the cavities, the total traction $\mathbf{t}(\mathbf{x},\omega) = \boldsymbol{\sigma}(\mathbf{x},\omega)\cdot\hat{\mathbf{n}}(\mathbf{x})$ has to vanish. Thus, we find a linear set of equations by satisfying the boundary condition on discrete matching points $\mathbf{x}$ at the boundary of the cavities. Along each cavity d, we have:

$$\mathbf{t}^{inc}(\mathbf{x},\omega) + \sum_{d=1}^{D}\sum_{p=1}^{P_d}\sum_{n=-N}^{+N}\left\{a_{pnd}\,\mathbf{t}^{\Phi}_{pnd}(\mathbf{x},\omega) + b_{pnd}\,\mathbf{t}^{\Psi}_{pnd}(\mathbf{x},\omega)\right\} + \mathbf{t}^{\varepsilon}(\mathbf{x},\omega) = \mathbf{0} \tag{B-6}$$

Generally, the resulting system of linear equation needs to be be solved in the least-squares sense by choosing more matching points than expansion functions.

Appendix C Asymptotic Elastic Free Surface

More realistic models of the earth should include the effect of the free surface which induces additional wave-phases interacting with scatterers. An analytical analysis of the free surface yields the following phases (Lapwood, 1949). For a source emanating P-waves, we have:

1. P, a P-wave propagating directly from the source to the receiver.
2. PP, a P-wave reflected as a P wave at the surface.
3. PS, a P-wave converted into a S-wave at the surface.
4. pSp, the surface S-wave which started and ended as a P wave but propagated along the surface as an S-wave. It does not satisfy a stationary-time criterion. It is a surface wave being confined to the near neighborhood of the free surface. It is not able to propagate itself and depends on energy supplied by the incident P wave. It is insignificant unless both source and receiver depths are small.
5. pS, the secondary S-wave which started as a P wave but converted into an S-wave at the interface. Contrarily to the PS-phase, it does not follow a stationary-time path. It is like the pSp except that the attenuation depends only on the source depth.
6. Rayleigh wave: R, a true surface wave which loses no energy to the interior of the elastic but proceeds with undiminished amplitude along the free surface.

Similarly, for a source generating S waves, we obtain:

7. S, the S-wave travelling directly from the source to the receiver.
8. SS, an S-wave reflected at the surface as an S-wave.
9. SP, an S wave converted into a P-wave at the surface.
10. sPs which started and ended as an S-wave, but travelled most of it's way as a P-wave along the surface. It is not a true surface wave but resembles a body wave being reflected twice at the surface. The path is a minimum time path where the wave propagated to and from the surface as an S wave, but as a P wave along the surface.
11. sP, the secondary P-wave which started as an S-wave but converted into a P-wave at the interface. Contrarily to the SP-phase, it does not follow a stationary-time path.
12. Rayleigh wave: Q. Similar to R, but generated by the incident S wave.

A schematic definition of these waves is presented in Figure 12. Of these waves, P, PP, PS, S, SS, and SP arise in the case of planar waves. The others are diffraction effects due to the curvature of the wave-fronts impinging on the free surface. In the special case of a receiver close to the surface, P, PP and PS combine, pS and pSp combine, S, sPs and SP combine, and S, SS, and sP combine.

Different techniques and methods exist to obtain the exact solution to the free surface problem. Instead of using the exact but costly solution, we sacrifice accuracy and derive asymptotic solutions which are numerically more efficient to evaluate. The main difference between the approximation and the exact solution will be the absence of some of the forementioned wave phases 1 – 12.

The most prominent phases induced by the free surface are the Rayleigh waves R and Q, and the primary reflections PP, PS, SP, and SS. We will concentrate on these phases and neglect all others. Describing P-waves as a function of a scalar potential ϕ where the displacement $\mathbf{u} = \nabla\phi$, we synthesize an arbitrary P-wave propagating toward the free surface by superposing all possible plane waves:

$$\phi = \frac{1}{\pi}\int_{-\infty}^{+\infty} \mathrm{w}(k,p)\frac{e^{ipx+i|h-z|\gamma}}{\gamma}\,dp\,, \tag{C-1}$$

where h and z denote the depths of source and receiver, respectively. Also, x is the horizontal distance between source and receiver. For a given wave number, $k = \omega/\alpha$, p and $\gamma = \sqrt{k^2 - p^2}$ are the tangential and normal component of the wave number with respect to the free surface. To satisfy the radiation condition, we choose the root such that $\Im m\,\gamma < 0$ for $z < 0$. Finally, $\mathrm{w}(k,p)$ is a weighting function which varies continuously and slowly with the argument p.

To satisfy the boundary conditions at the free surface, we need a P-wave as well as an S-wave propagating downwards. Describing the S-wave by a vector potential $\psi = \psi\hat{\mathrm{y}}$, we can again synthesize the fields by superposition:

$$\phi_{pp} = \frac{1}{\pi}\int_{-\infty}^{+\infty} \mathrm{w}(k,p)\,\mathrm{PP}(p)\frac{e^{ipx+i(h+z)\gamma}}{\gamma}\,dp\,, \tag{C-2}$$

$$\psi_{ps} = \frac{1}{\pi}\int_{-\infty}^{+\infty} \mathrm{w}(k,p)\,\mathrm{PS}(p)\frac{e^{ipx+ih\gamma+iz\delta}}{\gamma}\,dp\,, \tag{C-3}$$

where $\delta = \sqrt{l^2 - p^2}$ and $l = \omega/\beta$. Again we require that $\Im m\,\delta < 0$ for $z < 0$. The coefficients $\mathrm{PP}(p)$ and $\mathrm{PS}(p)$ are the reflection coefficients necessary to satisfy the boundary conditions along the free surface:

$$\mathrm{PP}(p) = \frac{4p^2\gamma\delta - \left[l^2 - 2p^2\right]^2}{4p^2\gamma\delta + \left[l^2 - 2p^2\right]^2} = -1 + \frac{8p^2\gamma\delta}{\mathrm{R}(p)} \tag{C-4}$$

$$\mathrm{PS}(p) = -\frac{4p\gamma\left[l^2 - 2p^2\right]}{4p^2\gamma\delta + \left[l^2 - 2p^2\right]^2} = -\frac{4p\gamma\left[l^2 - 2p^2\right]}{\mathrm{R}(p)} \tag{C-5}$$

where $\mathrm{R}(p) = 4p^2\gamma\delta + \left[l^2 - 2p^2\right]^2$ defines the Rayleigh function. At $p = p_r$ the Rayleigh function $\mathrm{R}(p)$ vanishes. The resulting singularity gives rise to an additional propagatory mode, the Rayleigh wave.

Similarly, we also synthesize the scalar potential of an arbitrary S-wave propagating toward the free surface by superposing all possible plane waves.

$$\psi = \frac{1}{\pi}\int_{-\infty}^{+\infty} \mathrm{w}(l,p)\frac{e^{ipx+i|h-z|\delta}}{\delta}\,dp \tag{C-6}$$

Again, to satisfy the boundary conditions at the free surface, we need a P-wave as well as an S-wave propagating downwards. Both fields are synthesized by superposition.

$$\phi_{sp} = \frac{1}{\pi}\int_{-\infty}^{+\infty} \mathrm{w}(l,p)\,\mathrm{SP}(p)\frac{e^{ipx+ih\delta+iz\gamma}}{\delta}\,dp \tag{C-7}$$

$$\psi_{ss} = \frac{1}{\pi}\int_{-\infty}^{+\infty} \mathrm{w}(l,p)\,\mathrm{SS}(p)\frac{e^{ipx+i(h+z)\delta}}{\delta}\,dp \tag{C-8}$$

The coefficients $\mathrm{SP}(p)$ and $\mathrm{SS}(p)$ are the reflection coefficients necessary to satisfy the boundary conditions along the free surface.

$$\mathrm{SP}(p) = \frac{4p\delta\left[l^2-2p^2\right]}{4p^2\gamma\delta+\left[l^2-2p^2\right]^2} = \frac{4p\delta\left[l^2-2p^2\right]}{\mathrm{R}(p)} \tag{C-9}$$

$$\mathrm{SS}(p) = \frac{4p^2\gamma\delta-\left[l^2-2p^2\right]^2}{4p^2\gamma\delta+\left[l^2-2p^2\right]^2} = -1+\frac{8p^2\gamma\delta}{\mathrm{R}(p)} \tag{C-10}$$

Instead of solving (C-2), (C-3) (C-7) and (C-8) exactly, we evaluate all integrals by the steepest decent approximation and add the contribution of the Rayleigh pole (Lapwood, 1949; Aki and Richards, 1980; DeSanto, 1992). Thus, for (C-2) we obtain:

$$\begin{aligned}
\phi_{pp} &\approx \int_{p_{pp}-\varepsilon}^{p_{pp}+\varepsilon} \mathrm{w}(k,p)\,\mathrm{PP}(p)\frac{e^{ipx+i(h+z)\gamma}}{\pi\gamma}\,dp \\
&\quad + \oint_{\Gamma} \mathrm{w}(k,p)\,\mathrm{PP}(p)\frac{e^{ipx+i(h+z)\gamma}}{\pi\gamma}\,dp \\
&= \sqrt{\frac{2}{\pi}\frac{1}{kr}}\,\mathrm{w}(k,p)\,\mathrm{PP}(p_{pp})e^{ip_{pp}x+i(h+z)\gamma_{pp}-i\frac{\pi}{4}} \\
&\quad + 2\pi i\ \mathrm{Res}\left(\mathrm{w}(k,p)\,\mathrm{PP}(p)\frac{e^{ipx+i(h+z)\gamma}}{\pi\gamma}\right)\Bigg|_{p=p_r} \\
&= \sqrt{\frac{2}{\pi}\frac{1}{kr}}\,\mathrm{w}(k,p)\,\mathrm{PP}(p_{pp})e^{ip_{pp}x+i(h+z)\gamma_{pp}-i\frac{\pi}{4}} \\
&\quad + \mathrm{w}(k,p)\frac{2ip_r\delta_r}{\gamma_r\delta_r-(l^2-2p_r^2)}e^{ip_rx+i(h+z)\gamma_r}
\end{aligned} \tag{C-11}$$

where $r = \sqrt{x^2 + (h+z)^2}$ and p_{pp} denotes the saddle point of (C-2) located at $p_{pp} = kx/r$.

Similarly, the P to S conversion (C-3) yields

$$\begin{aligned}\psi_{ps} \approx \sqrt{\frac{2}{\pi}\frac{1}{kr_p + lr_s\xi_s}}\,\mathrm{w}(k,p)\,\mathrm{PS}(p_{ps})e^{ip_{ps}x + ih\gamma_{ps} + iz\delta_{ps} - i\frac{\pi}{4}} \\ - \mathrm{w}(k,p)\,\mathrm{sgn}\,(x)\,i\frac{l^2 - 2p_r^2}{\gamma_r\delta_r - (l^2 - 2p_r^2)}e^{ip_r x + ih\gamma_r + iz\delta_r}\end{aligned} \tag{C-12}$$

where $p_{ps} = kx_p/r_p$, $r_p = \sqrt{x_p^2 + h^2}$, $r_s = \sqrt{x_s^2 + z^2}$, $x_s = x - x_p$, $\xi_s = \frac{\gamma^2}{\delta^2}$ and $0 < x_p < x$ is given by

$$\begin{aligned}(\alpha^2 - \beta^2)x_p^4 - 2x(\alpha^2 - \beta^2)x_p^3 + \left[\alpha^2(x^2 + h^2) - \beta^2(x^2 + z^2)\right]x_p^2 - \\ 2x\alpha^2h^2x_p + x^2\alpha^2h^2 = 0\end{aligned} \tag{C-13}$$

which is numerically solved using a Newton-Raphson algorithm (Press *et al.*, 1988).

For the S to P conversion (C-7), we obtain

$$\begin{aligned}\phi_{sp} \approx \sqrt{\frac{2}{\pi}\frac{1}{lR_r + kR_p\xi_p}}\,\mathrm{w}(l,p)\,\mathrm{SP}(p_{sp})e^{ip_{sp}x + ih\delta_{sp} + iz\gamma_{sp} - i\frac{\pi}{4}} \\ + \mathrm{w}(l,p)\,\mathrm{sgn}\,(x)\,i\frac{l^2 - 2p_r^2}{\gamma_r\delta_r - (l^2 - 2p_r^2)}e^{ip_r x + ih\delta_r + iz\gamma_r}\end{aligned} \tag{C-14}$$

where $p_{sp} = lX_s/R_s$, $R_s = \sqrt{X_s^2 + h^2}$, $R_p = \sqrt{X_p^2 + z^2}$, $X_p = x - X_s$, $\xi_p = \frac{\delta^2}{\gamma^2}$ and $0 < X_s < x$ is given by

$$\begin{aligned}(\alpha^2 - \beta^2)X_s^4 - 2x(\alpha^2 - \beta^2)X_s^3 + \left[\alpha^2(x^2 + z^2) - \beta^2(x^2 + h^2)\right]X_s^2 + \\ 2x\beta^2h^2X_s - x^2\beta^2h^2 = 0\end{aligned} \tag{C-15}$$

which is again solved numerically using a Newton-Raphson algorithm.

Finally, the S to S reflection (C-8) yields

$$\begin{aligned}\psi_{ss} \approx \sqrt{\frac{2}{\pi}\frac{1}{lr}}\,\mathrm{w}(l,p)\,\mathrm{SS}(p_{ss})e^{ip_{ss}x + i(h+z)\delta_{ss} - i\frac{\pi}{4}} \\ + \mathrm{w}(l,p)\frac{2ip_r\gamma_r}{\gamma_r\delta_r - (l^2 - 2p_r^2)}e^{ip_r x + i(h+z)\delta_r}\end{aligned} \tag{C-16}$$

where $r = \sqrt{x^2 + (h+z)^2}$ and p_{ss} denotes the saddle point of (C-8) located at $p_{ss} = lx/r$.

Setting the weighting function $\mathrm{w}(k,p) = 1$, we recognize in equation (C-1) the well-known identity (Chew, 1990)

$$H_0(kr) = \frac{1}{\pi}\int_{-\infty}^{+\infty}\frac{e^{ipx + i|z-h|\gamma}}{\gamma}\,dp \tag{C-17}$$

where $r^2 = x^2 + (z-h)^2$. By using the raising or lowering operators $\mathcal{R}(k)$ and $\mathcal{L}(k)$ (Chew, 1990) as weighting functions $\mathrm{w}(k,p)$, we obtain the solution to sources of different angular order $H_{|n|}(kr)e^{in\theta}$. More specifically, the operators $\mathcal{R}(k)$ and $\mathcal{L}(k)$ raise, respectively lower, the angular order of a solution by one:

$$H_n(kr)e^{in\theta} = \mathcal{R}^n(k)H_0(kr) \qquad n \geq 0\,, \tag{C-18}$$

$$H_{|n|}(kr)e^{in\theta} = \mathcal{L}^{|n|}(k)H_0(kr) \qquad n \leq 0\,. \tag{C-19}$$

A little calculation involving the recurrence relations of Bessel functions (Abramowitz and Stegun, 1964) and equation (C-17) shows that the following expressions define the operators.

$$\mathcal{R}(k) = -\frac{1}{k}\left[\frac{\partial}{\partial x} + i\frac{\partial}{\partial z}\right] = -\frac{ip-\gamma}{k} \tag{C-20}$$

$$\mathcal{L}(k) = -\frac{1}{k}\left[\frac{\partial}{\partial x} - i\frac{\partial}{\partial z}\right] = -\frac{ip+\gamma}{k} \tag{C-21}$$

To simplify the notation, we introduce an alternative raising and lowering operator.

$$\mathfrak{R}^n(k) = \begin{cases} \mathcal{R}^n(k) & \text{for } n > 0 \\ 1 & \text{for } n = 0 \\ \mathcal{L}^{|n|}(k) & \text{for } n < 0 \end{cases} \tag{C-22}$$

Thus, replacing $\mathrm{w}(k,p)$ by $\mathfrak{R}^n(k)$ in equations (C-11) and (C-12) allows us to estimate the effect of the free surface on a compressional cylindrical solution of arbitrary angular order n. Similarly, replacing $\mathrm{w}(l,p)$ by $\mathfrak{R}^n(l)$ in equations (C-14) and (C-16) yields the contributions of the free surface to the rotational solution of order n.

For a compressional source of order n located at $\mathbf{x}_d = (0,h)$, we obtain the following expression for the displacement by combining (C-1), (C-11), and (C-12).

$$\begin{aligned}
\mathbf{u}_n^{\Phi}(\mathbf{x},\mathbf{x}_d) =& \nabla\Big(H_{|n|}(kr)e^{in\theta}\Big) + \\
& \nabla\Big(\sqrt{\frac{2}{\pi}\frac{1}{kr}}\,\mathfrak{R}^n(k)\,\mathrm{PP}(p_{pp})e^{ip_{pp}x+i(h+z)\gamma_{pp}-i\frac{\pi}{4}}\Big) + \\
& \nabla\Big(\mathfrak{R}^n(k)\frac{2ip_r\delta_r}{\gamma_r\delta_r-(l^2-2p_r^2)}e^{ip_rx+i(h+z)\gamma_r}\Big) + \\
& \nabla\times\Big(\sqrt{\frac{2}{\pi}\frac{1}{kr_p+lr_s\xi_s}}\,\mathfrak{R}^n(k)\,\mathrm{PS}(p_{ps})e^{ip_{ps}x+ih\gamma_{ps}+iz\delta_{ps}-i\frac{\pi}{4}}\Big)\hat{\mathbf{y}} - \\
& \nabla\times\Big(\mathfrak{R}^n(k)\,\mathrm{sgn}\,(x)\,i\frac{l^2-2p_r^2}{\gamma_r\delta_r-(l^2-2p_r^2)}e^{ip_rx+ih\gamma_r+iz\delta_r}\Big)\hat{\mathbf{y}}
\end{aligned} \tag{C-23}$$

For a rotational source of order n located at $\mathbf{x}_d = (0, h)$, we obtain the following expression for the displacement by combining (C-1), (C-16), and (C-14).

$$
\begin{aligned}
\mathbf{u}_n^{\Phi}(\mathbf{x}, \mathbf{x}_d) =& \nabla \times \left(H_{|n|}(lr) e^{in\theta} \right) \hat{\mathbf{y}} + \\
& \nabla \times \left(\sqrt{\frac{2}{\pi} \frac{1}{lr}}\, \Re^n(l)\, \mathrm{SS}(p_{ss}) e^{ip_{ss}x + i(h+z)\delta_{ss} - i\frac{\pi}{4}} \right) \hat{\mathbf{y}} + \\
& \nabla \times \left(\Re^n(l) \frac{2ip_r\gamma_r}{\gamma_r\delta_r - (l^2 - 2p_r^2)} e^{ip_r x + i(h+z)\delta_r} \right) \hat{\mathbf{y}} + \\
& \nabla \left(\sqrt{\frac{2}{\pi} \frac{1}{lR_s + kR_p\xi_p}}\, \Re^n(l)\, \mathrm{SP}(p_{sp}) e^{ip_{sp}x + ih\delta_{sp} + iz\gamma_{sp} - i\frac{\pi}{4}} \right) + \\
& \nabla \left(\Re^n(l)\, \mathrm{sgn}\,(x)\, i \frac{l^2 - 2p_r^2}{\gamma_r\delta_r - (l^2 - 2p_r^2)} e^{ip_r x + ih\delta_r + iz\gamma_r} \right)
\end{aligned}
\tag{C-24}
$$

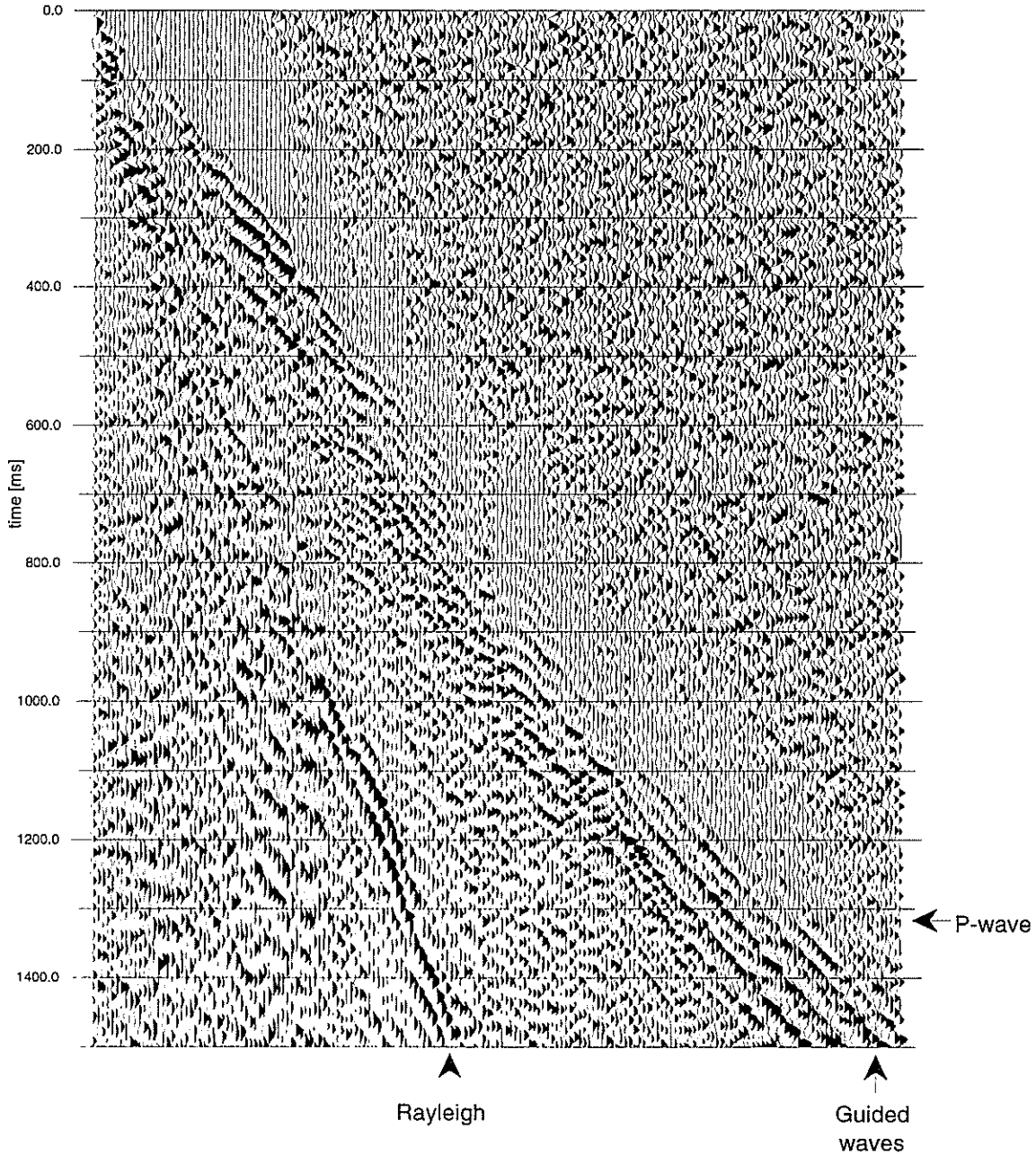

Figure 1: The first 1.5 s of the seismogram shot with the source located in the valley at station 1045. Shown are the traces located between station 1045 and 1221.

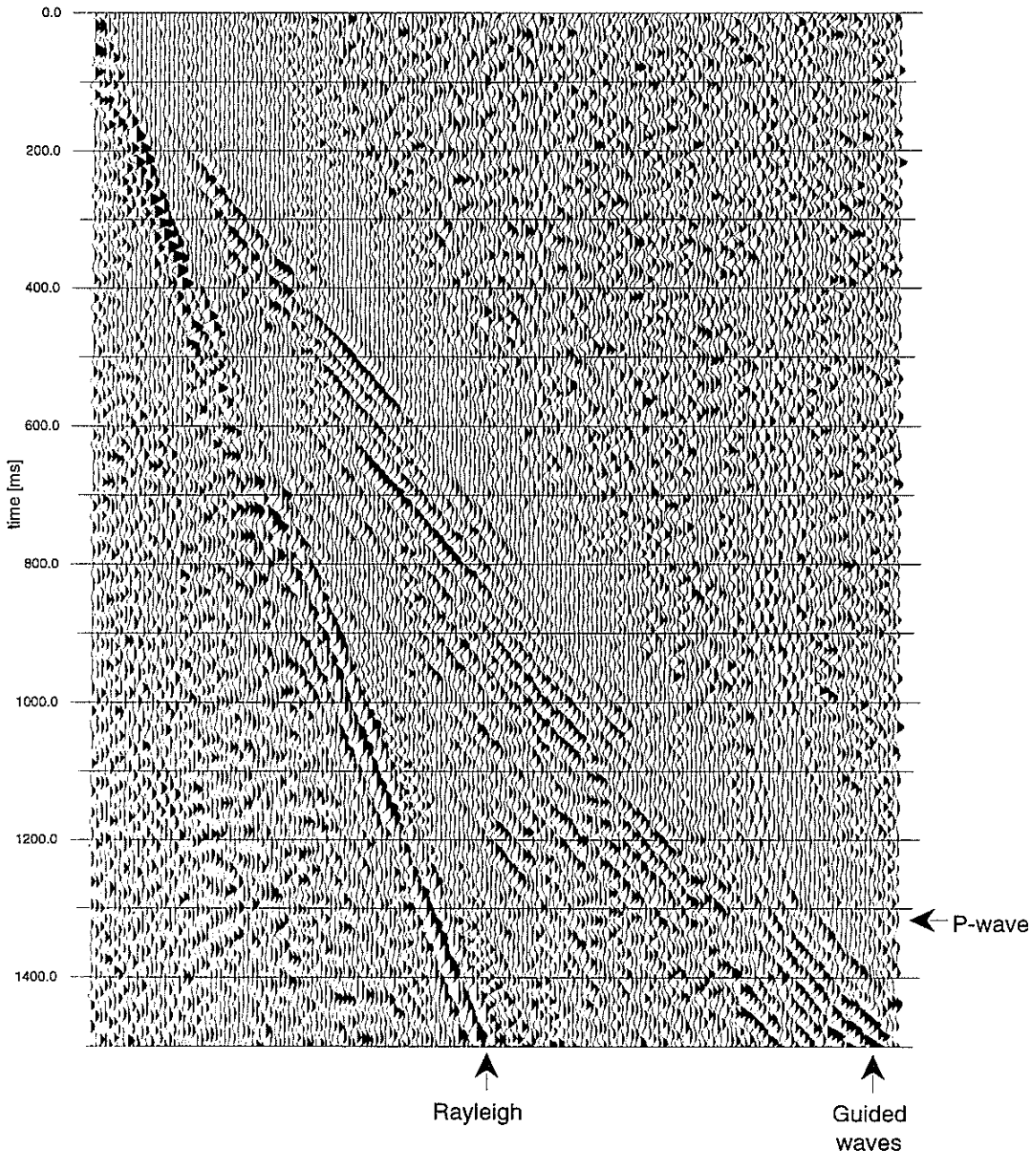

Figure 2: The first 1.5 s of the seismogram shot with the source on top of the mesa at station 1153. Shown are the traces located between station 1153 and 1329.

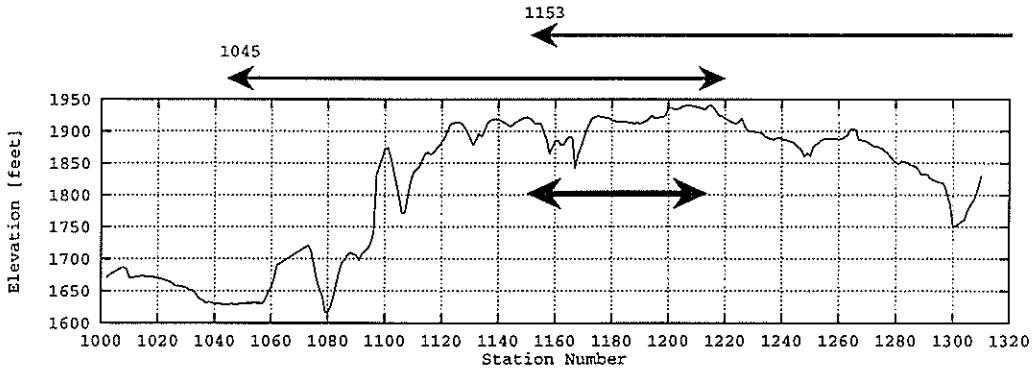

Figure 3: Elevation as a function of station number for the seismic dataset. The vertical exaggeration is 25 : 1. The distance between stations is 110 ft.A slow and heterogeneous surface layer exists for elevations lower than 1750 ft. For higher elevations, a fast and more homogeneous limestone is exposed at the surface. Thin arrows indicate the receiver locations for the example records 1045 and 1153. The bold arrow denotes the receivers used for detailed analysis of record 1156.

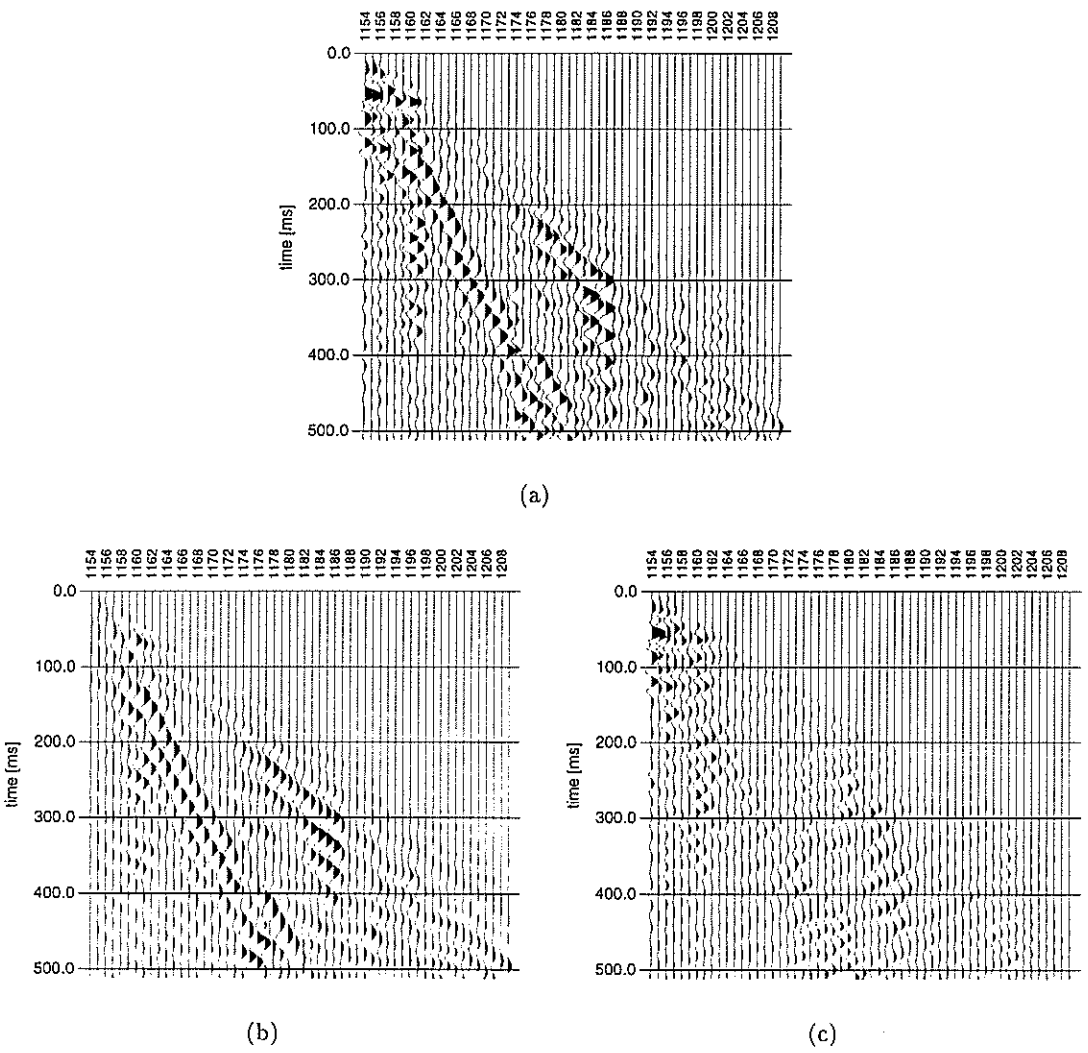

Figure 4: Details of field record 1153. Only the first 56 receivers and the first 512 ms are shown: (a) total field record, (b) forward propagating waves, and (c) backward propagating waves. All seismograms are scaled equally.

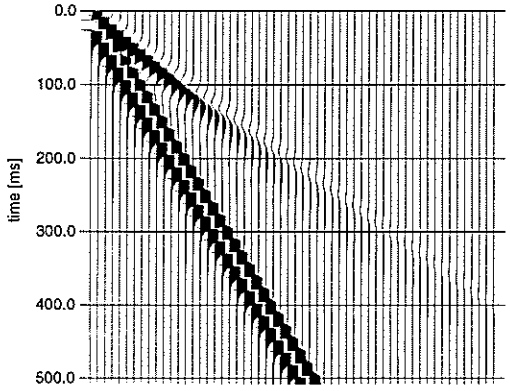

Figure 5: Flat free-surface: vertical displacement calculated for a pointforce at surface location 1153 at a nominal depth of 10 m.

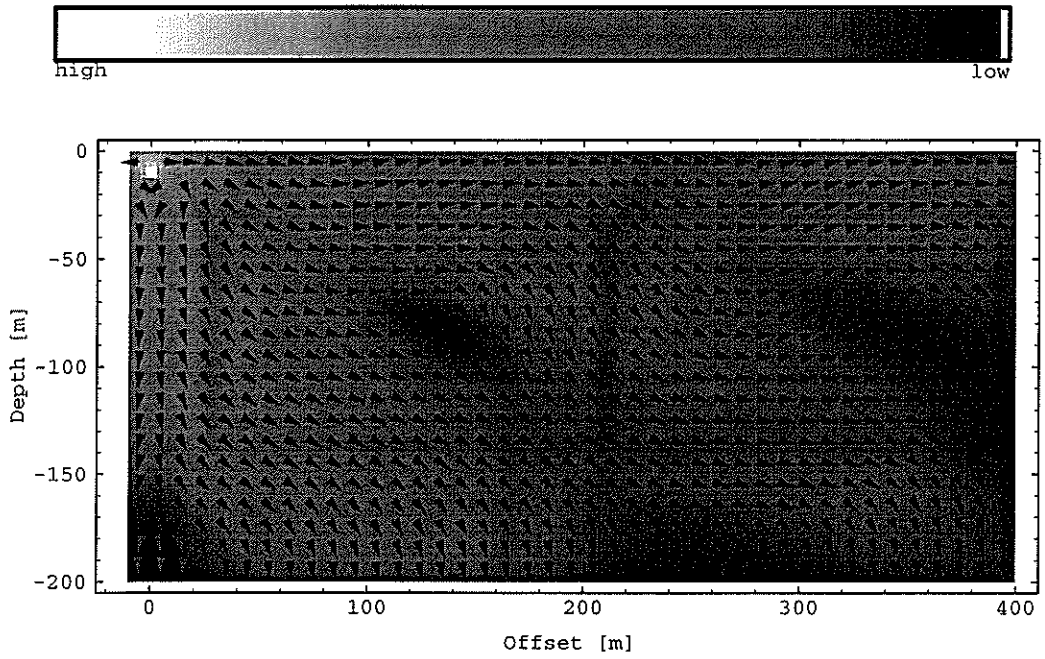

(a)

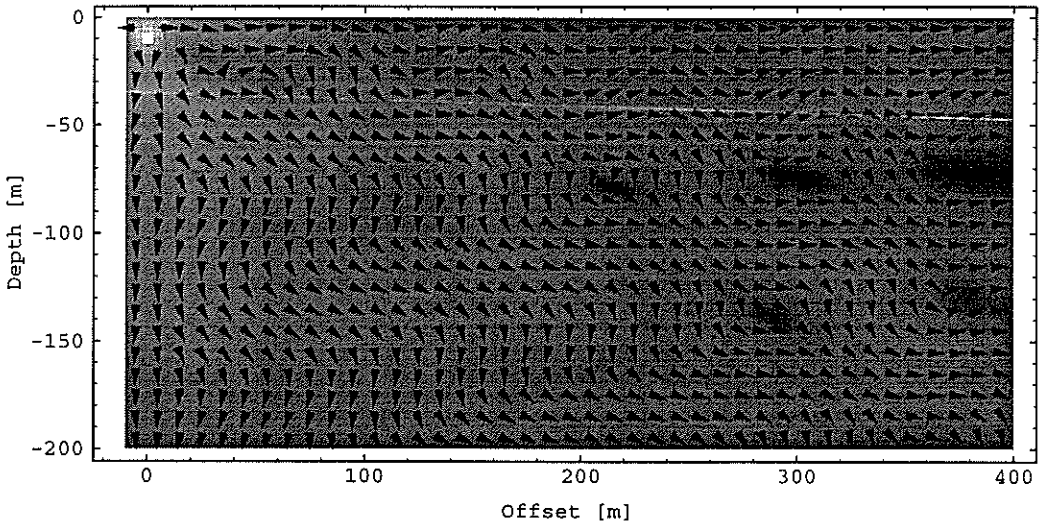

(b)

Figure 6: Flat free-surface: energy-density $E(\mathbf{x},\omega)$ and energy-flux vector $\mathbf{S}(\mathbf{x},\omega)$ for the total wavefield at (a) 20 Hz and (b) 45 Hz.

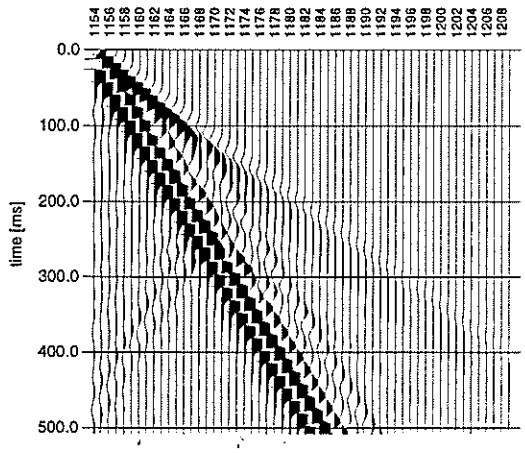

Figure 7: Rough free-surface: vertical displacement calculated for a pointforce at surface location 1153 at a nominal depth of 10 m.

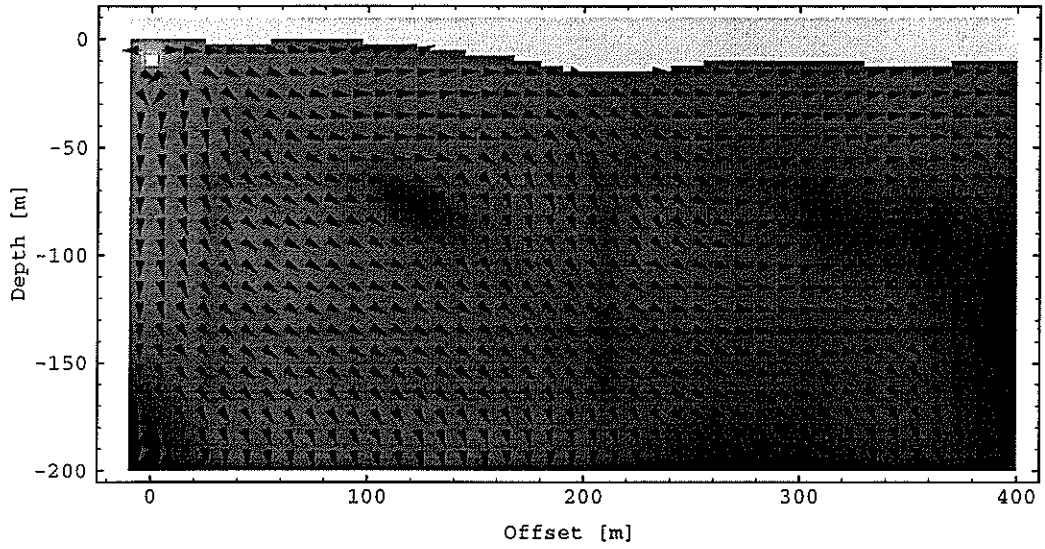

(a)

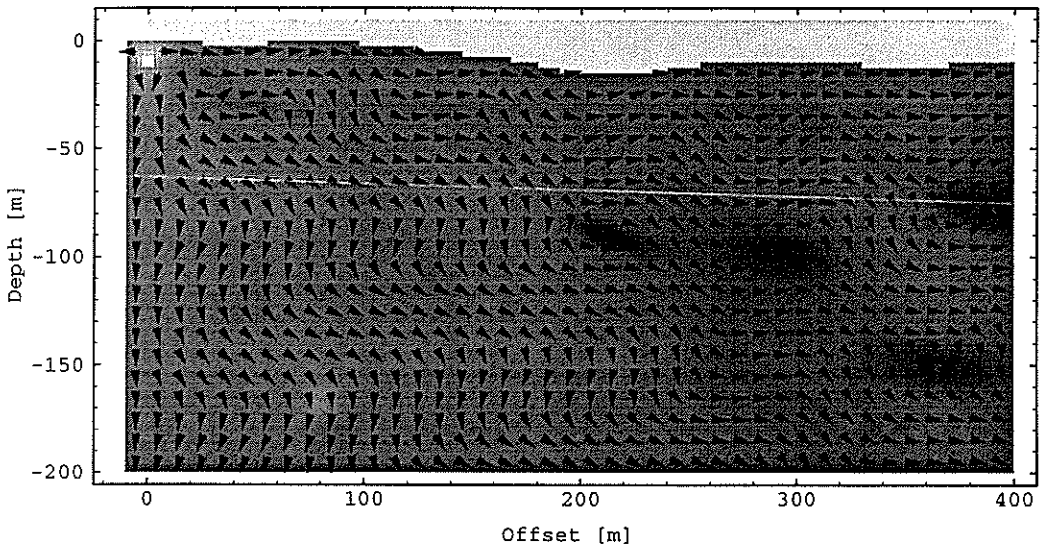

(b)

Figure 8: Rough free-surface: energy-density $E(\mathbf{x}, \omega)$ and energy-flux vector $\mathbf{S}(\mathbf{x}, \omega)$ for the total wavefield at (a) 20 Hz and (b) 45 Hz. The bright yellow indicates pixel above the topography.

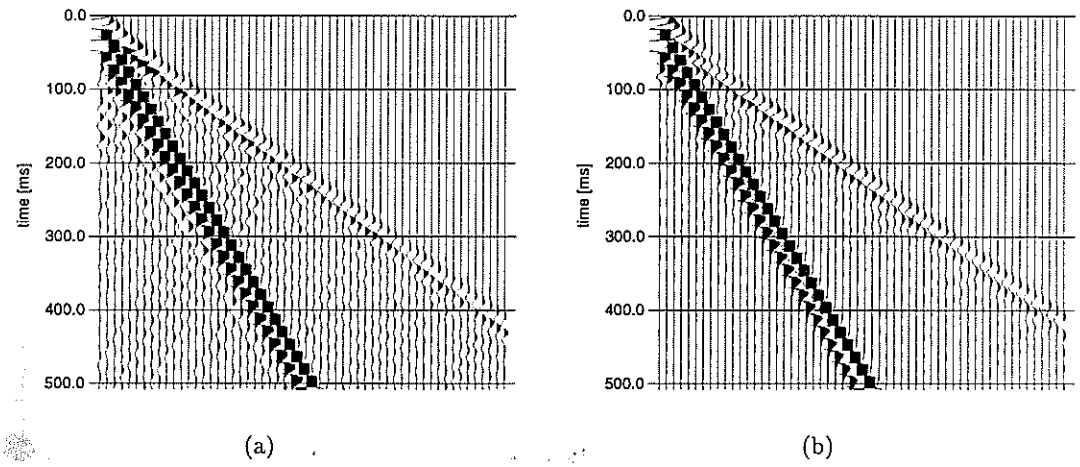

Figure 9: Heterogeneous near-subsurface: vertical displacement calculated for a point-force at surface location 1153 at a nominal depth of 10 m: (a) distribution of heterogeneities with average depth of 25 m, and (b) with average depth of 80 m.

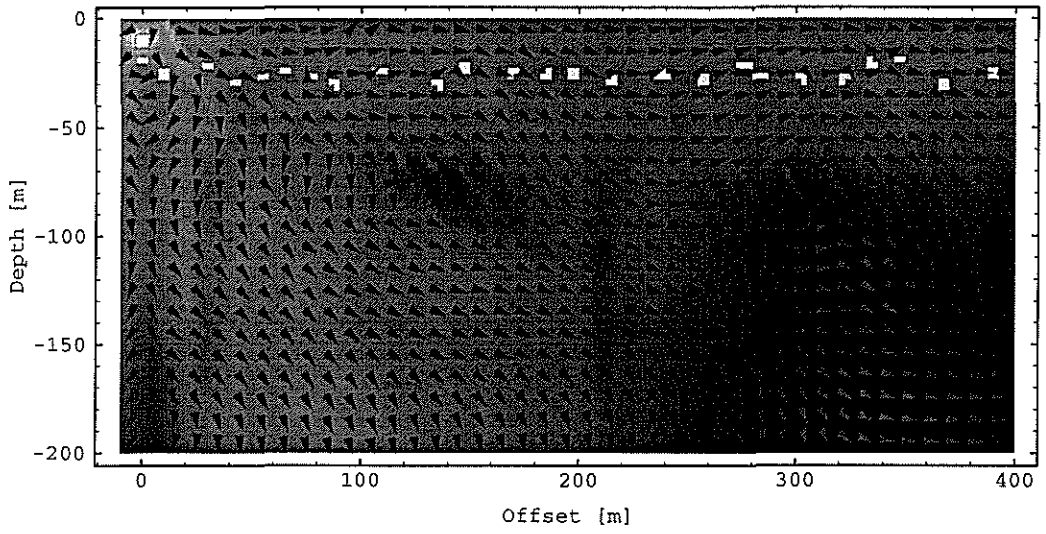

(a)

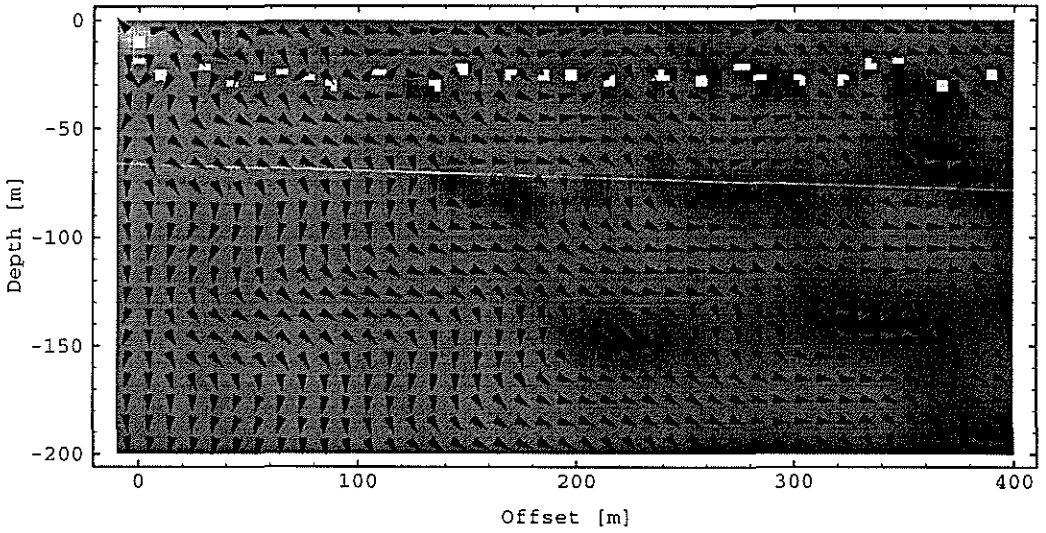

(b)

Figure 10: Heterogeneous near-subsurface: energy-density $E(\mathbf{x},\omega)$ and energy-flux vector $\mathbf{S}(\mathbf{x},\omega)$ for the total wavefield at (a) 20 Hz and (b) 45 Hz. The yellow speckles indicate the locations of the heterogeneities at an average depth of 25 m.

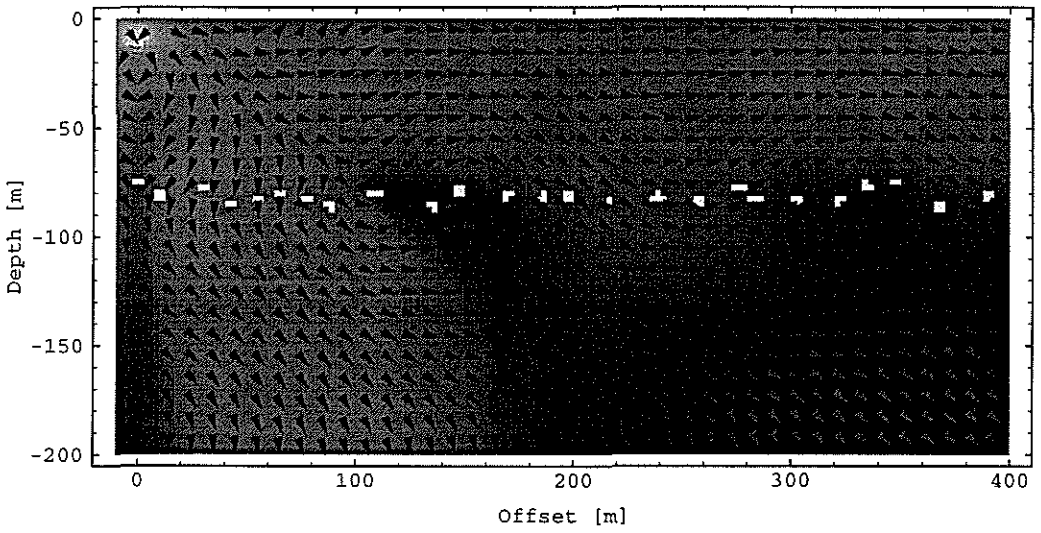

(a)

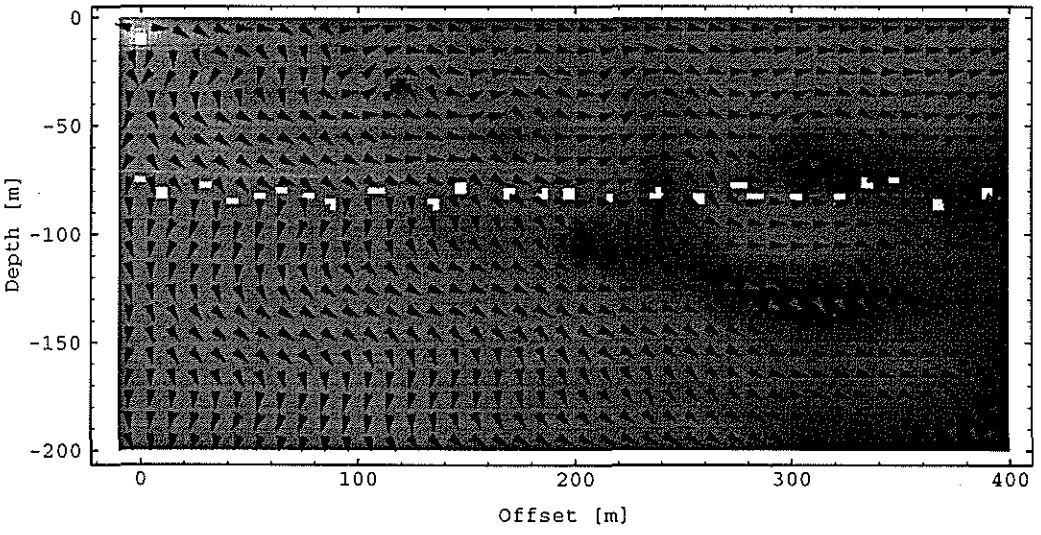

(b)

Figure 11: Heterogeneous near-subsurface: energy-density $E(\mathbf{x},\omega)$ and energy-flux vector $\mathbf{S}(\mathbf{x},\omega)$ for the total wavefield at (a) 20 Hz and (b) 45 Hz. The yellow speckles indicate the locations of the heterogeneities at an average depth of 80 m.

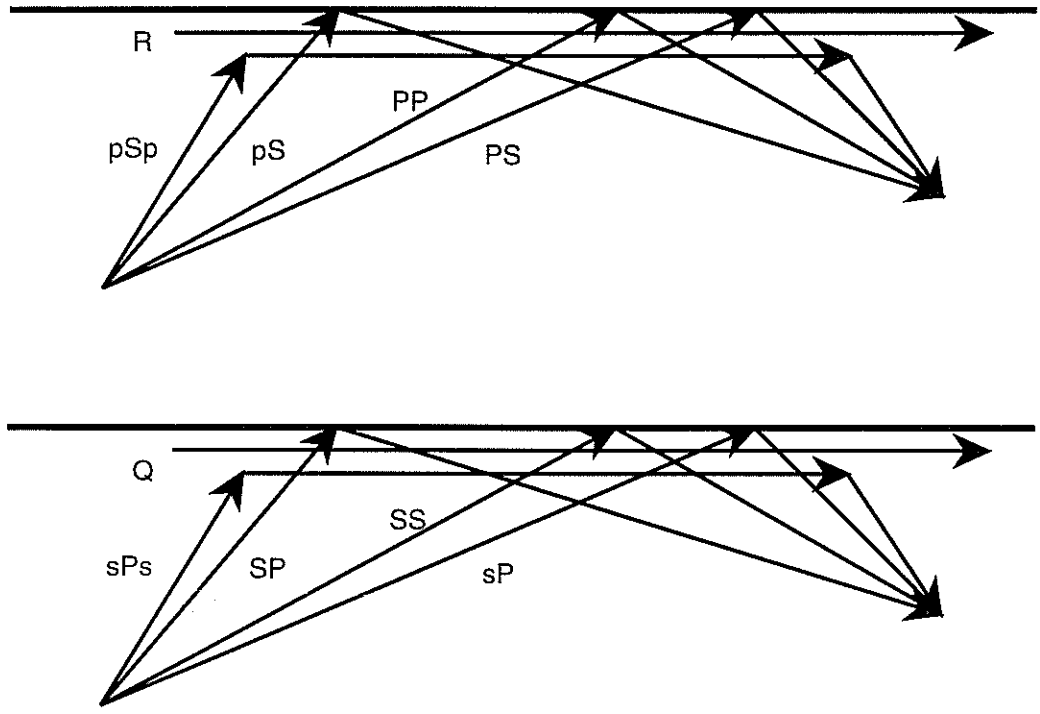

Figure 12: A summary of elastic waves which propagate due to the interaction of an incident wave and the free surface. PP, PS, SP and SS arise in the case of reflection of plane waves. All others are diffraction effects due to the curvature of the wavefronts impinging on the free surface (Lapwood, 1949).